processes

MDPI

Article

Coordinated Control of Thermal Power Unit–Hybrid Energy Storage System for AGC Based on Improved Markov Power Prediction

Junci Tang [1], Miao Wang [1], Zhenqi Ye [2], Jiahao Fan [3,*], Feng Hong [3], Qi Jia [2], Dan Pei [2] and Yi Shao [2]

[1] State Grid Liaoning Electric Power Co., Ltd., Shenyang 110002, China
[2] State Grid Liaoning Electric Power Research Institute, Shenyang 110006, China
[3] School of Control and Computer Engineering, North China Electric Power University, Beijing 102206, China
* Correspondence: fanjh@ncepu.edu.cn

Abstract

High penetration of renewable energy poses severe frequency stability challenges to modern power systems, while conventional thermal power units (TPUs) fail to satisfy high-precision frequency regulation demands due to slow dynamic response. A hybrid energy storage system (HESS) with a flywheel and battery has become a mainstream scheme for TPU-HESS coordinated regulation by realizing complementary advantages. However, existing strategies generally adopt rigid state-of-charge (SOC) constraints, lack battery lifespan optimization, and suffer from incomplete power prediction models with weak integration with real-time control. To fill these gaps, this paper proposes a prediction-assisted coordinated control framework. A three-matrix adaptive Markov prediction model corrected by K-means time-series morphological clustering is established, combined with a weighted random sampling scenario tree method. Furthermore, a prediction-driven dynamic SOC interval feedforward-feedback control strategy is designed for HESS power dispatch and SOC management. Simulations verify that the clustering correction reduces prediction RMSE by 22.25%. The proposed strategy increases the optimal SOC operation ratio of batteries by 34.25%, decreases equivalent cycles by 19.80%, and lifts the comprehensive AGC performance index by 160.93%. This study provides technical support for efficient and durable TPU-HESS frequency regulation systems.

Keywords: automatic generation control; hybrid energy storage system; Markov chain; K-means clustering

Check for updates

Academic Editor: Hsin-Jang Shieh

Received: 25 August 2026
Revised: 8 October 2026
Accepted: 16 October 2026
Published: 22 October 2026

Copyright: © 2026 by the authors. Licensee MDPI, Basel, Switzerland. This article is an open access article distributed under the terms and conditions of the Creative Commons Attribution (CC BY) license.

1. Introduction

By the end of 2025, after the installed capacity of wind power and solar photovoltaic power generation surpassed that of coal-fired power units, it further exceeded the total installed capacity of thermal power units (TPUs) and the national maximum electricity load, reaching 1.842 billion kilowatts [1]. However, the inherent intermittency, volatility, and randomness of renewable energy output exacerbate grid power disturbances and frequency fluctuations, bringing severe challenges to the safe and stable operation of modern power systems [2]. Currently, TPUs undertake the primary frequency regulation tasks of power systems. Restricted by large thermal inertia, delayed mechanical response, and limited regulation accuracy, traditional TPU cannot independently satisfy the high-frequency, stochastic, and variable-amplitude regulation demands under high renewable energy penetration scenarios [3].

Rapid development of emerging energy storage technologies, including battery energy storage systems (BESSs) and flywheel energy storage systems (FESSs), provides effective technical support for improving the frequency regulation performance of TPUs. The coordinated coupling of TPUs and energy storage systems can mechanically compensate for the inherent frequency regulation limitations of TPUs [4]. Nevertheless, single-type energy storage faces inherent bottlenecks in frequency regulation applications: high investment costs limit capacity deployment scale, while frequent repetitive charge–discharge operations triggered by automatic generation control (AGC) commands significantly degrade equipment service life. By contrast, a hybrid energy storage system (HESS) combining an FESS and a BESS realizes complementary advantages for frequency regulation. An FESS tolerates frequent rapid power regulation with negligible aging despite high unit costs, while a BESS features an economical large-capacity configuration and is susceptible to performance decay under intensive charge–discharge cycles. The hybrid configuration maximizes the respective strengths of the two energy storage types and has become a mainstream optimization scheme for TPU-HESS system regulation [5].

Extensive investigations have been carried out worldwide on TPU-HESS system frequency regulation strategies. Latif et al. [6] reviewed advanced controllers and mainstream algorithms for load frequency management (LFM) in renewable-dominated power systems. Sun et al. [7] proposed an online optimal control method to mitigate capacity waste caused by conventional full-power compensation, which improves energy storage utilization and frequency regulation performance. However, this method adopts rigid state-of-charge (SOC) limit logic, which easily induces secondary frequency disturbances when energy storage operates near threshold boundaries. Hong et al. [8] presented a modal matching-based AGC auxiliary control strategy for TPU using HESS, which applies a dynamic pre-limitation interval for energy storage output but fails to optimize lithium battery cycle life via power prediction. In practical engineering, Xie et al. [9] implemented a 2 MW BESS-based AGC auxiliary regulation project at Beijing Shijingshan Thermal Power Plant. The single-energy-storage scheme neglects coordinated control between continuous frequency regulation output and SOC self-recovery, resulting in low effective operating duration of energy storage equipment. For hybrid energy storage scheduling, Wang et al. [10] realized power task allocation for FESS-BESS hybrid systems via wavelet decomposition, whereas lithium batteries bear long-term low-frequency regulation tasks without corresponding lifecycle optimization. Sun et al. [11] further adopted Haar wavelet transform to decouple high- and low-frequency power components of hybrid energy storage, fully utilizing the high-power response advantages of FESS. Overall, existing single and hybrid thermal-storage coordinated control strategies rely merely on real-time operating states of TPU and adopt rigid SOC constraint logic, lacking targeted lithium battery cycle life optimization and full consideration of future HESS power demand.

Accurate power prediction for energy storage demand is the core foundation for energy management formulation, output optimization, and SOC regulation [12]. Markov chain-based power prediction and scenario tree-based uncertainty optimization have been widely studied for power system stochastic optimization. Existing studies have made preliminary progress in Markov-based power prediction, yet they suffer from systematic defects in modeling completeness and engineering applicability. He et al. [13] verified the effectiveness of Markov chain prediction models but only constructed two-state transition matrices corresponding to AGC power rise and fall conditions, ignoring unit steady-state operating scenarios within the frequency regulation dead band and failing to integrate prediction models with real-time control [14]. Shen et al. [15] adopted an adaptive online learning hidden Markov model for power prediction but did not couple forecasting results with practical real-time control loops. In terms of model optimization, Li et al. [16]

combined clustering algorithms with improved Markov chains to address the stationary distribution problem of traditional models, yet the single Markov modeling framework excludes scenario tree-based multi-scenario optimization, causing loss of probability distribution information. Dong et al. [17] adopted scenario reduction methods but only retained maximum-probability single scenarios, leading to excessive smoothing of prediction results and poor adaptability to stochastic energy storage power fluctuations. For data clustering preprocessing, Liu et al. [18] applied the K-means algorithm for photovoltaic weather clustering. The purely algorithm-driven initialization and amplitude-dominated Euclidean distance criterion easily cause misclustering of time series with inconsistent variation trends, degrading the representativeness of typical power curves. Overall, existing Markov power prediction models lack complete transition matrix modeling covering unit steady-state operating conditions, multi-scenario optimization design, and effective integration with real-time closed-loop control. In addition, the conventional K-means clustering method suffers from unstable initial centroid initialization and amplitude-biased matching, which deteriorates clustering accuracy.

To sum up, five prominent deficiencies remain in current relevant research and will be overcome in this paper: TPU coupled with hybrid energy storage mostly adopt real-time state-based control with rigid SOC limiting logic and no targeted lithium battery cycle life optimization; the future power demand of HESS is not taken into account; incomplete Markov transition matrices without coverage of steady power operating conditions; power forecasting is not combined with real-time closed-loop control, and multi-scenario layouts are missing in Markov matrix construction; K-means has unstable initial centroids and amplitude-biased matching that causes misclustering and unrepresentative typical curves.

To fill the aforementioned research gaps, this paper develops a holistic power prediction and energy management framework for HESS-assisted thermal AGC regulation, combining a clustering-improved adaptive Markov prediction model and a prediction-oriented dynamic SOC closed-loop control strategy. The main contributions are summarized as follows:

(1) A three-matrix adaptive Markov chain model with real-time updating is proposed. By constructing separate state transition and macroscopic trend probability matrices, the model effectively characterizes the non-stationary and stochastic features of short-term frequency regulation power fluctuations.
(2) A weighted random sampling-based scenario tree optimization method is established. Combined with variable-time-domain sampling and scenario pruning, the method preserves valid probabilistic distribution information while significantly reducing computational overhead.
(3) A K-means time-series morphological clustering-based secondary correction strategy is designed. A refined historical power sample database is constructed to calibrate raw prediction results and improve the accuracy and robustness of stochastic power prediction.
(4) A prediction-driven SOC dynamic interval feedforward-feedback control strategy is proposed. This strategy enables flexible HESS output limiting, avoids battery overcharge and overdischarge, and maintains SOC in a healthy range, thereby extending the service life of hybrid energy storage devices.

The rest of this paper is organized as follows. Section 2 establishes the power prediction model based on the K-means clustering-corrected adaptive Markov model, andproposes a coordinated control strategy for hybrid energy storage system (HESS) power allocation and further designs the dynamic SOC recovery control strategy. In Section 3, comparative simulation experiments are carried out to comprehensively evaluate the prediction accuracy of

the proposed model, as well as the AGC performance and lithium battery life improvement effect. Finally, Section 4 concludes this paper.

2. Materials and Methodology

2.1. Materials

The dataset was obtained from a 330 MW thermal power unit participating in AGC regulation in Shandong Province. The sampling interval was 1 s, and the chronological dataset contained 345,600 samples collected during four typical summer days. The measured physical signals were the AGC dispatch command P_{AGC} and the actual active power output of the thermal power unit P_{TPU}. The HESS regulation demand was derived as $P_{\mathrm{d}} = P_{\mathrm{AGC}} - P_{\mathrm{TPU}}$. The FESS power, BESS power, and their SOC trajectories were generated by the proposed coordinated-control model rather than directly measured in the field. This distinction is maintained throughout the following analysis.

The complete chronological dataset was divided into training, validation, and test subsets with proportions of 70%, 15%, and 15%, respectively. No random shuffling was applied in order to prevent future information leakage. The initial transition matrices were estimated only from the training subset. The validation subset was used to select the adaptive update interval, correction-fusion weights, and other hyperparameters, whereas the test subset was used exclusively for final performance evaluation.

Software and Computational Environment. All data preprocessing, Markov chain modeling, K-means clustering, scenario-tree generation, HESS coordinated-control simulations, and performance evaluations were implemented in MATLAB. The simulations were conducted on a personal computer equipped with [Intel Core i5-10300H], [32 GB RAM], and [Windows 10 64-bit]. MATLAB [R2024a] was used as the primary computational platform.

2.2. Power Prediction Methodology for HESS

2.2.1. Markov Chain Theory

As a classical stochastic process with the memoryless property, the Markov chain is applicable for modeling HESS power demand, as the future power state is dominantly determined by its current value rather than historical trajectories [18].

The energy storage demand power is defined as $P_{\mathrm{c}} = P_{\mathrm{AGC}} - P_{\mathrm{TPU}}$, and its positive value is the energy storage discharge. Let P_{AGC} denote the AGC command and P_{TPU} denote the active power of the thermal unit. Denote the discrete state set of HESS power demand as $P_{\mathrm{d}} = \left\{ {P_{\mathrm{d}}}^1,\ {P_{\mathrm{d}}}^2,\ \cdots,{P_{\mathrm{d}}}^s \right\}$, $\forall {P_{\mathrm{d}}}^i \in \mathbf{R}$, with s discrete states. $\mathbf{R}$ is the set of real numbers. The full power operating range is uniformly discretized at a fixed step size to span the entire HESS demand range. Let the demand power at time k denote $P_{\mathrm{d}}(k)$; if the demand power at time $k+1$ is regarded as a random process to establish a prediction model, then the element T_{ij} in the Markov state transition matrix $\boldsymbol{T} \in \boldsymbol{R}^{s \times s}$ can be expressed as follows [13]:

$$\begin{cases} T_{ij} = Pr\left[P_d(k+1) = P_d^j \mid P_d(k) = P_d^i\right] \\ T_{ij} = \frac{m_{ij}}{m_i} \\ m_i = \sum m_{ij} \end{cases} \quad \forall ij \in \{1, 2, \cdots, s\} \tag{1}$$

where m_{ij} counts the transitions from state i to state j across the dataset, and m_i is the total transition count from state i. The physical meaning of Equation (1) is that, given demand power ${P_d}^i$ at time k, the probability that the demand power equals ${P_d}^j$ at time k+1 is T_{ij}. The transition probability can be determined via maximum likelihood estimation with historical prior information. Given a sufficiently large sample set, the state occurrence frequency converges to the transition probability.

The probability distribution of HESS demand power at time step k is defined as a $1 \times s$ row vector $P(k)$. Using the transition matrix, the distribution at the next time step $P(k+1)$ is given by the following [13]:

$$P(k+1) = \boldsymbol{T}P(k)' \tag{2}$$

2.2.2. Principles of Trend Identification

With a preset frequency regulation deadband threshold, the power signal is classified into rising, steady, and falling trend states for the construction of the three-matrix Markov model. Power variations within the threshold are categorized as steady state, whereas variations exceeding the upper and lower thresholds are marked as rising and falling states, respectively. This threshold-based partitioning conforms to practical AGC operating characteristics of a TPU. It suppresses frequent state transitions induced by measurement noise and differentiates steady-state operation within the frequency regulation deadband from actual power regulation behaviors. Combined with the established macroscopic trend matrix, the probability distribution of future power trends can be acquired to capture non-stationary power evolution characteristics and boost power prediction accuracy [16]. The HESS power demand data used in this work are obtained from a TPU in Shandong Province, with the trend distribution shown in Figure 1.

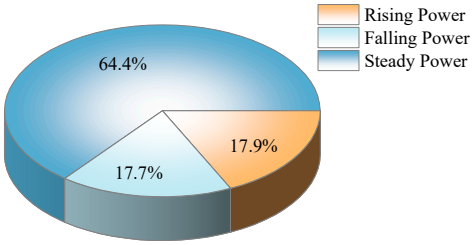

Figure 1. Trend sample distribution.

Based on the statistical distribution of the power change rates in the dataset, and in conjunction with the unit's AGC deadband setting and power measurement accuracy, the trend discrimination threshold is determined as $1.5\%P_e$/min, i.e., 0.0825 MW/s for the unit considered in this study, where P_e denotes the rated power of the thermal power unit. Accordingly, the power sequences are divided into three trend states: rising, steady, and falling, with the overall trend distribution presented in Figure 1. On this basis, three independent AGC state transition matrices, denoted as T_{up}, T_{st}, and T_{down}, are constructed for the three trend states.

2.2.3. Adaptive Update Method for the Transition Matrix

Daily AGC commands exhibit notable temporal variations driven by load characteristics, with stronger regulation during daytime and weaker fluctuations overnight. Given the divergent fluctuation features of these commands, TPUs differ significantly in dynamic response performance. An adaptive updating mechanism is employed to enhance Markov model accuracy, where an exponential correction factor amplifies the weight of the latest deviations to better track power variation patterns. The specific steps are as follows [13]:

1. First, the transition matrix T is calculated from historical HESS power data, and the following steps are iterated in real time for each sampling time point k.

2. For the current time step k, assume that the demand power corresponds to the discrete state j, and that the demand power at time step $k-1$ corresponds to the discrete

state i. Calculate the transition probability δ_i by counting the number of transitions within the most recent time window.

$$\delta_i = \frac{n_{ij}}{n_i} \forall j \in \{1, 2, \cdots, s\} \tag{3}$$

where n_{ij} is the number of times the power discrete state transitioned from i to j during the previous D_T window; n_i is the total number of times the power discrete state transitioned from i to other states.

3. Calculate the exponential correction factor.

$$\delta_i' = \exp\left\{\lambda\left[\delta_i - T_{adpi}(k-1)\right]\right\} \tag{4}$$

where λ is the adaptive learning coefficient, which can be adjusted based on its impact on prediction accuracy; $T_{adpi}(k-1)$ is the state transition probability at time $k-1$ for row i of T_{adp}.

Once the adaptive learning coefficient λ is set, the model calculates the difference between the probabilities estimated over the most recent time window and the transition matrix at the previous time step, thereby enabling the adaptive transition matrix to learn recent patterns. Specifically, it updates each element $p_{ij}(k)$ in row i of T_{adp} using the calculated δ_i':

$$p_{ij}'(k) = \delta_{ij}' p_{ij}(k-1) \forall j \in \{1, 2, \cdots, s\} \tag{5}$$

4. Each row of the adaptive matrix T_{adp} should be normalized to maintain the standardization of probabilities as follows:

$$T_{adpi} = \frac{p_{ij}'(k)}{\sum_{j=1}^{s} p_{ij}'(k)} = \frac{\delta_{ij}' p_{ij}(k-1)}{\sum_{j=1}^{s} \delta_{ij}' p_{ij}(k-1)} \tag{6}$$

After normalization, the adaptive matrix T_{adp} accurately captures recent patterns following the adaptive update, thereby maintaining the model's state-of-the-art performance.

Let $P_{\mathrm{d}} = \left\{{P_{\mathrm{d}}}^1, {P_{\mathrm{d}}}^2, \cdots, {P_{\mathrm{d}}}^s\right\}$, $\forall {P_{\mathrm{d}}}^i \in \mathbf{R}$ denote the discretization operator that maps the continuous HESS demand power into one of s states with a resolution of 1/3 MW. Three initial transition matrices, T_{up}, T_{st}, and T_{down}, were estimated from the training data according to the trend label of ΔP_{d}. At each sampling instant, only the preceding D_T-hour data window was used to calculate the recent transition-frequency matrix. The adaptive matrix was then updated using Equations (3)–(6) and normalized row-wise. Hence, the prediction procedure consists of offline estimation of the initial matrices and causal online adaptation based solely on previously observed samples.

2.2.4. Scenario Tree Generation

The scenario probability distribution at the next instant can be derived from the transition matrix. If no screening is conducted during node construction, the number of energy storage demand power rises exponentially with discrete states s, inducing heavy computation with trivial control gains [13].

This paper develops a variable prediction horizon scenario tree algorithm. Probability thresholds are preset to prune low-probability branches early and extend high-probability ones, enabling shorter branch horizons than the target. Separate stepwise thresholds further cut computational cost. Combined with weighted random sampling that mines transition matrix information, the method optimizes scenario screening and yields a scenario tree capped by maximum nodes $\pi_{\max}$.

First, define the variables and sets: The nth step of the prediction uses the transition matrix T_n. The probability distribution for transitions from node N_x to other states is $P(N_{xj})\ \forall j \in \{1, 2, \cdots, s\}$. The node probability is ε_x (starting from the initial root node); its parent node is $N_{pre}(x)$, and its child nodes are $N_{suc}(x)$. The tree nodes consist of discrete power states, i.e., the sets $N = \{N_0, N_1, \cdots\}$, and Figure 2 illustrates a scenario tree generation diagram.

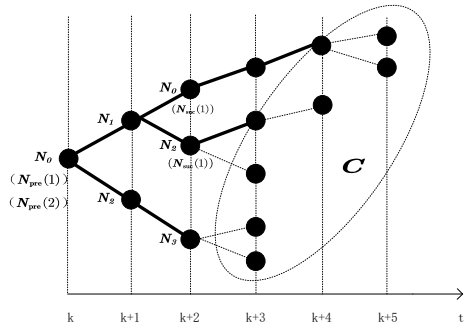

Figure 2. Schematic diagram of variable-prediction time-domain scenario tree generation.

The scene tree generation process is proposed in this study as follows:

Threshold filters are configured to prune low-probability scenarios and accelerate computation. The state transition matrices T_n differ drastically across prediction steps; multi-step predictions are derived via matrix multiplication, and probability distributions gradually disperse with extended horizons. Accordingly, individual transition probability thresholds β_n are assigned to each step, where the threshold value of β_n shall exceed the corresponding prediction horizon.

The root node is initialized as N_0 with an initial node probability $\varepsilon_0 = 1$ and node count $\pi = 1$. Starting from N_0, child nodes $N_{suc}(x)$ are extracted. Combined with the adaptive Markov transition matrix T_{adp} and threshold β_1, the candidate node set $C = \{N_{suc}(1)\}$ and corresponding probability values are acquired. Iterate Steps (3)–(5) until the maximum allowed node number π_{max} is reached to terminate scenario tree construction.

When selecting the π-th node corresponding to the n-th prediction step, the total probability of all selected nodes is not equal to unity. Accordingly, the probability of each element c_j in set C shall be normalized as follows:

$$P'(c_j) = \frac{P(c_j)}{\sum P(c_j)} \tag{7}$$

And the cumulative weight is calculated as follows:

$$P_{accu}(c_j) = \sum_{m=1}^{j} P'(c_m) \tag{8}$$

Use the random function $r = rand(0, 1)$ to select a node c_i^*, where i is as follows:

$$i = \begin{cases} argmax\left(P_{accu}(c_j) < r\right) & r > P_{accu}(c_i) \\ 1 & r \le P_{accu}(c_i) \end{cases} \tag{9}$$

The node probability for node c_i^* is shown as Equation (10):

$$\mathcal{E}_{c_i^*} = \mathcal{E}_{N_{pre}(c_i^*)} P(c_j) \tag{10}$$

Eliminate the selected node c_i^* from candidate set C. If the prediction horizon of c_i^* is shorter than the preset N_P, its child nodes satisfying threshold β_n are appended to C via the Markov transition matrix, as shown below:

$$C = \left(C \backslash c_i^*\right) \cup \{N_{suc}(c_i^*)\}, \pi = \pi + 1 \tag{11}$$

The scenario tree constructed via the above approach explicitly records all energy storage demand power together with their occurrence probabilities. Fundamentally, this multi-scenario model supplies power demand prediction data for the subsequent flywheel–lithium HESS frequency regulation control strategy.

2.2.5. K-Means Clustering and Prediction Correction

As a classic unsupervised clustering algorithm, K-means is extensively adopted to categorize time-series operating condition samples. Different from conventional single-point clustering, this work extracts segmented mean features to characterize power curve morphology, which suppresses single-point noise. Combined with the silhouette coefficient, the optimal cluster number is determined. Typical power fluctuation patterns are categorized to build a historical sample library for precise prediction correction, offsetting the memoryless defect of Markov chains. The silhouette coefficient calculation formula is given below [16].

$$S(i) = \frac{b(i) - a(i)}{\max\{b(i), a(i)\}} \tag{12}$$

where $a(i)$ denotes the average distance from sample i to other samples in the same cluster, quantifying intra-cluster cohesion; $b(i)$ stands for the average distance between sample i and its nearest sample from alien clusters, measuring inter-cluster separation. The silhouette coefficient $S(i)$ derived from $a(i)$ and $S(i)$ ranges from [1, −1]. A value of $S(i)$ approaching 1 signifies higher intra-cluster similarity and distinct inter-cluster boundaries, yielding superior clustering performance.

After the K-means clustering is completed, each cluster center corresponds to a typical power profile W_k that characterizes the standard variation mode of all time-series samples within the cluster. In the rolling prediction framework of the Markov chain model, a fixed-length sliding window is adopted to extract segmented time-series features. We compute the mean discrepancies among the front, middle, and rear segments to match the input curve against patterns stored in the correction library. This method exploits full-window feature information and suppresses single-point noise interference. Once pattern matching finishes, historical samples with power values close to the real-time operating point are retrieved from the matched cluster. Their average value serves as the correction term, and weighted fusion is implemented to output the ultimate predicted power. The corresponding formula is proposed in this study as follows:

$$P_{final} = \alpha P_{markov} + \beta P_{correct} \tag{13}$$

where P_{final} denotes the final corrected power prediction, P_{markov} represents the predicted output of the Markov chain model, and $P_{correat}$ is the correction term derived from similar clustered samples. α, β denote the weights of the baseline prediction and the correction term, respectively, subject to the constraint $\alpha + \beta = 1$. The weights satisfy $\alpha + \beta = 1$. They were selected by a grid search on the validation set, where $\alpha \in \{0, 0.1, \cdots, 1\}$ and $\beta = 1 - \alpha$. The selected pair, $(\alpha, \beta) = [0.7, 0.3]$, yielded the minimum validation RMSE and was fixed for all test cases.

The output of the adaptive Markov model is subsequently used as the direct input to scenario-tree generation and multi-step HESS demand-power prediction, thereby establishing the prediction interface between the measured AGC signals and the control layer.

2.3. Coordinated Control Methodology

2.3.1. Model Framework of This Paper

The adaptive Markov model provides the multi-step HESS demand-power prediction used to preview future FESS/BESS SOC trajectories, which directly supports the subsequent feedforward-feedback coordinated control. This chapter designs a corresponding frequency regulation control strategy as illustrated in Figure 3.

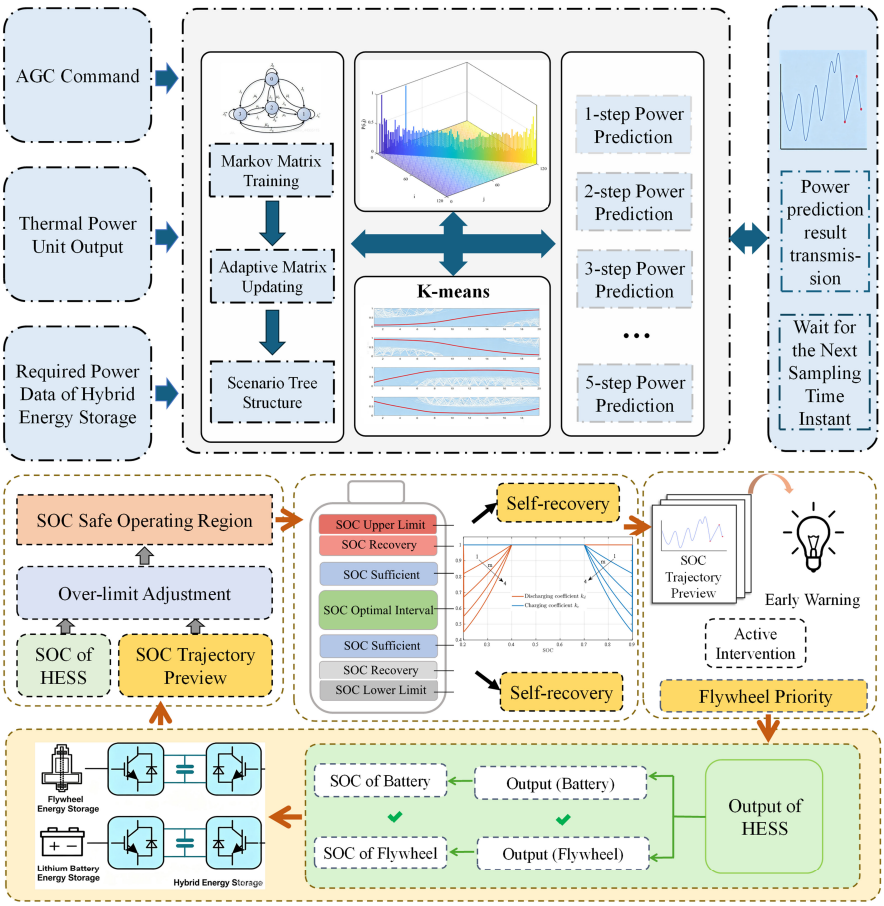

Figure 3. Control strategy framework of TPU-HESS system.

As shown in Figure 3, the block diagram systematically illustrates the principle of the proposed strategy integrating power prediction feedforward and dynamic SOC interval management. Taking the difference between the AGC command and the actual output of the TPU as the HESS demand power, the system simultaneously acquires real-time SOC and safe operating intervals of FESS and BESS, which serve as boundary constraints for subsequent prediction and control.

The prediction layer (upper section of the diagram), built upon the K-means clustering-corrected adaptive Markov model proposed in Chapter 2, generates a rolling sequence of multi-step energy storage demand power predictions for 1–5 steps ahead [19]. The prediction outputs not only directly support power allocation in the current control cycle but also act as a key feedforward signal forwarded to the decision-making layer.

The decision-making layer (middle section) feeds the multi-step power predictions into the storage energy iteration equation in real time to project future SOC trajectories. If

the projected trajectory is determined to enter the charge recovery or discharge recovery interval within several upcoming sampling cycles, the system triggers a warning flag and issues an "active interruption" command to the execution layer (lower section).

On this basis, the execution layer proactively corrects the power command of the current cycle. Specific measures include implementing prediction-deviation-based adaptive attenuation of charge and discharge coefficients (i.e., soft limiting control) for BESS, and activating the flywheel self-recovery strategy that prioritizes deploying the flywheel to undertake high-frequency small-amplitude fluctuations and low-power recovery tasks. This mechanism transforms the traditional passive protection mode of post-limit-violation hard cutoff into a feedforward control paradigm of pre-limit-violation active intervention.

Furthermore, a feedback correction loop, comprising limit violation adjustment and SOC feedback, is embedded in the architecture, forming a coordinated closed-loop framework of "prediction feedforward guidance + real-time SOC feedback correction". Finally, the revised power commands are dispatched to FESS and BESS, respectively, for execution, and the aforementioned rolling optimization procedure is repeated at the next sampling instant.

2.3.2. HESS Power Allocation

1. Dynamic Response Phase

The required power of the HESS is defined as the deviation between the AGC dispatch instruction and the actual active power output of the TPU. A positive value corresponds to the discharging state, whereas a negative value represents the charging state.

In the AGC response stage, to accelerate the command tracking speed and maximize the respective merits of flywheel and battery energy storage, the flywheel is assigned priority for rapid power regulation, and the battery energy storage undertakes residual power compensation. Accordingly, a power threshold-based fixed distribution strategy is formulated in this study: low-power regulation tasks are undertaken solely by the flywheel; for high-power demands, the flywheel operates at its rated power limit, and the battery energy storage supplements the residual power deficit.

$$P_f = \begin{cases} P_e \ , & |P_e| < P_D \\ P_{fn} \ , & P_e > P_D \\ -P_{fn} \ , & -P_e > P_D \end{cases} \tag{14}$$

$$P_b = \begin{cases} 0 \ , & |P_e| < P_D \\ \min(|P_e - P_{fn}|, P_{bn}) \ , & P_e > P_D \\ -\min(|P_e - P_{fn}|, P_{bn}) \ , & -P_e > P_D \end{cases} \tag{15}$$

where P_f and P_b are the power commands for flywheel energy storage and battery energy storage, respectively; P_{fn} and P_{bn} are the rated powers of flywheel energy storage and battery energy storage, respectively; P_e is the difference between the AGC command and the unit's output power, where a positive value indicates discharge and a negative value indicates charging; P_D is the flywheel output threshold.

2. Steady State Maintenance Phase

To cut down the equivalent cycling times of lithium-ion batteries for service life prolongation and take full advantage of the infinite cycling durability of flywheel energy storage, the flywheel undertakes all regulation tasks during the steady-state stage. The

battery energy storage maintains zero power output except when its SOC falls within the mandatory recovery interval.

$$P_f = P_e \tag{16}$$

$$P_b = 0 \tag{17}$$

2.3.3. SOC Recovery Control

Long-term continuous operation of the HESS may cause the battery energy storage to reach full charge or deep discharge. Such overcharged and over-discharged states degrade the sustained frequency regulation capacity of the energy storage system. To address this issue, an SOC dynamic interval management strategy for HESS is proposed in this work, which optimizes frequency regulation performance while realizing autonomous SOC recovery control [8].

SOC is expressed in per unit, with 1 representing 100%. As illustrated in Figure 4, the SOC operating domain of the energy storage system is partitioned into five intervals according to practical engineering operation features and battery cycle life constraints.

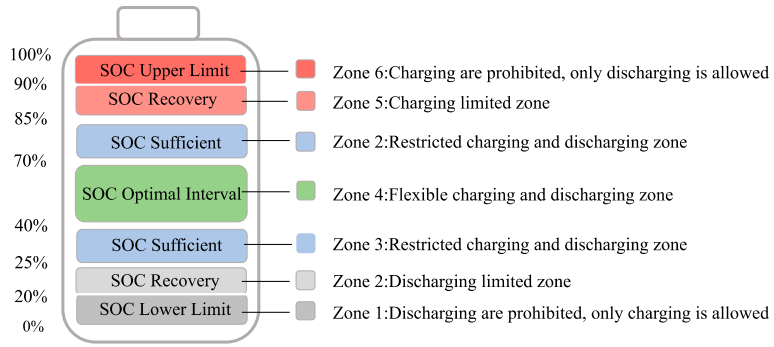

Figure 4. Schematic diagram of battery SOC classification intervals.

1. FESS Self-Recovery Strategy

FESS consists of a mechanical rotor supported by magnetic bearings and inevitably produces steady-state power losses during operation [11]. Consequently, the SOC, which is characterized by the rotational speed of the flywheel, will gradually decline under standby conditions without supplementary power compensation, further weakening its full-power frequency regulation capability [20].

To tackle this problem, a FESS autonomous SOC recovery strategy is proposed in this study. It relies on predicted outputs of the Markov chain model to predict SOC variation within the prediction horizon. Once the SOC approaches the lower recharge threshold, low-power charging compensation is activated to restore the flywheel to the normal healthy SOC interval. If the SOC exceeds the upper discharge recovery threshold, the flywheel executes slight discharging to reserve sufficient margin for subsequent charging instructions. The power instruction rules for the flywheel self-recovery scheme are proposed below.

- When the SOC change within the prediction time window reaches the charging recovery range,

$$P_{fd} = \begin{cases} -k_f \cdot P_{fn}, & 0 < S_f < 0.25 \\ P_f, & 0.25 < S_f < 0.85 \end{cases} \tag{18}$$

- When the SOC change within the prediction time window reaches the discharge recovery range,

$$P_{fc} = \begin{cases} P_f, & 0.25 < S_f < 0.85 \\ k_f \cdot P_{fn}, & 0.85 < S_f < 1 \end{cases} \tag{19}$$

where P_{fd} and P_{fc} denote the discharge and charging power commands of the flywheel, which are constrained by the flywheel SOC limits; k_f is the self-recovery adjustment coefficient; S_f refers to the real-time SOC of the flywheel energy storage; P_{fn} stands for the flywheel rated power; and P_f represents the normal regulation power instruction of the flywheel.

2. BESS Self-Recovery Strategy

An adaptive SOC regulation strategy is proposed by introducing exponentially decaying charging and discharging coefficients, which are defined as follows [21]:

- When SOC < 0.4, the discharging coefficient decays exponentially with the reduction in SOC to limit the discharge depth and avoid excessive SOC drop. The mathematical expression of the discharging coefficient k_d is given in Equation (20):

$$k_d = \begin{cases} e^{-m\cdot(0.4-S_b)}, 0.2 < S_b < 0.4 \\ 1, 0.4 < S_b < 0.9 \end{cases} \quad (20)$$

- When SOC > 0.7, the charging coefficient decays exponentially as SOC increases, reducing the charging power to prevent a sharp rise in SOC; the expression for the charging coefficient k_c is as follows:

$$k_c = \begin{cases} e^{-m\cdot(S_b-0.7)}, 0.7 < S_b < 0.9 \\ 1, 0.2 < S_b < 0.7 \end{cases} \quad (21)$$

where S_b represents the real-time SOC of the battery energy storage; m represents the dynamic self-recovery rate coefficient. When SOC < 0.2, forced charging is enabled and k_d equals 0; when SOC > 0.9, forced discharging is enabled and k_c equals 0.

Figure 5 illustrates the attenuation characteristic curves of Charging-Discharging coefficients with m ranging from 1 to 4. When the SOC deviates from its optimal operating interval, the system modulates the charge–discharge coefficients accordingly to restore the SOC to the target optimal range.

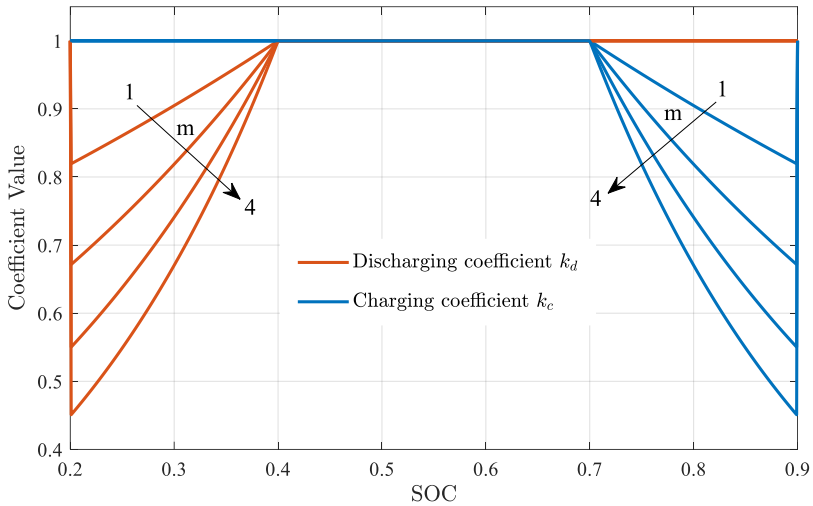

Figure 5. Attenuation characteristics curve of the charging/discharging coefficient.

- When SOC is within the optimal range of 0.4 to 0.7, the coefficient is 1, and the battery participates in frequency regulation at full power.

Based on the above charge–discharge coefficient settings, when the battery energy storage is discharging,

$$P_{bd} = \begin{cases} -k_b \cdot P_{bn}, & 0 < S_b < 0.25 \\ k_d \cdot P_b, & 0.25 < S_b < 0.85 \end{cases} \quad (22)$$

- When the battery energy storage is charging,

$$P_{bc} = \begin{cases} k_c \cdot P_b, & 0.25 < S_b < 0.85 \\ k_b \cdot P_{bn}, & 0.85 < S_b < 1 \end{cases} \quad (23)$$

where P_{bd} and P_{bc} represent the discharge and charge commands, respectively, subject to the battery energy storage's SOC constraints; k_b is the battery energy storage's self-recovery coefficient; P_{bn} is the battery energy storage's rated power; P_b is the power command during normal operation; the discharge coefficient is k_d; the charge coefficient is k_c.

Lithium-ion batteries are subject to finite charge–discharge cycle life, so daily cycle degradation control is essential for long-term operation. In practical engineering, the equivalent cycle number $N_L(P)$ is widely adopted to quantitatively evaluate the aging effect induced by control strategies. A complete equivalent cycle consists of one full charging process and one full discharging process, calculated as follows:

$$N_L(P) = \sum [\, P_{l,d}(t) + P_{l,c}(t)]/C_n \quad (24)$$

where $P_{l,d}(t)$ and $P_{l,c}(t)$ represent the discharge power and charge power of the battery energy storage, respectively; C_n is the rated capacity of the battery energy storage. Using the rainflow counting method [8], different numbers of charge and discharge cycles are converted to equivalent cycle counts $N_L(P)$, considering only the impact of the battery's own depth of discharge D_x on the number of cycles [22]. The corrected equivalent cycle count $N_L(D_x)$ is obtained as follows:

$$N_L(D_x) = N_L(P)\left(\frac{D_x}{D_b}\right)^{0.19} e^{1.69(1-D_x/D_b)} \quad (25)$$

where D_b is the reference depth of discharge for lithium-ion batteries, set to 0.8 based on engineering experience. Equation (25) is used as a post-event degradation assessment metric and is not directly embedded in the real-time control optimization. Battery life protection in the online controller is achieved indirectly through dynamic SOC intervals and adaptive charge/discharge attenuation [22].

2.3.4. Feedforward-Feedback Integrated Control

Conventional closed-loop SOC regulation adopts passive lagging feedback control, which cannot preemptively suppress the risk of SOC over-limit violation. In this work, the previously established Markov chain power prediction model is utilized to acquire short-term predicted power sequences over the prediction horizon. On this basis, the prospective SOC evolution trajectory of the battery energy storage system is deduced, and a feedforward-feedback integrated soft constraint control strategy is proposed. The recursive formula for calculating the battery future SOC trajectory is expressed as follows:

$$\begin{cases} \Delta E(i) = \text{pred}_{\text{series}}(i) \cdot \frac{1}{3600} \\ SOC_{\text{temp}}(i) = SOC_{\text{temp}}(i-1) - \frac{\Delta E(i)}{b_{\text{capacity}}} \end{cases} \quad (26)$$

where $\mathrm{pred}_{\mathrm{series}}(\mathrm{i})$ denotes the predicted power at the i-th moment within the prediction window; $\Delta \mathrm{E}(\mathrm{i})$ represents the predicted energy variation (MWh) at step i; $\mathrm{SOC}_{\mathrm{temp}}(\mathrm{i})$ is the iterative estimated SOC at step i; $\mathrm{b}_{\mathrm{capacity}}$ stands for the rated capacity of the battery energy storage pack.

Relying on the iteratively updated predicted SOC trajectory, an over-limit pre-warning logic is constructed. Considering the battery dynamic response delay, a 5% SOC margin is set as the warning threshold δ_{th}:

$$\begin{cases} \psi_L = 1 & ,\mathrm{SOC}_{\mathrm{temp}} \leqslant \mathrm{SOC}_{\mathrm{min}} + \delta_{\mathrm{th}} \\ \psi_H = 1 & ,\mathrm{SOC}_{\mathrm{temp}} \geqslant \mathrm{SOC}_{\mathrm{max}} - \delta_{\mathrm{th}} \end{cases} \tag{27}$$

where ψ_L and ψ_H are the flag bits indicating that the SOC is about to fall below the lower limit and exceed the upper limit, respectively; $\mathrm{SOC}_{\mathrm{min}}$ and $\mathrm{SOC}_{\mathrm{max}}$ are the critical values at which the SOC enters the recovery zone; and δ_{th} is the 5% SOC threshold for the early warning boundary.

The optimized flywheel self-recovery strategy upgrades the scheme in Section 3.3 by replacing pure real-time SOC judgment with predictive SOC information for pre-recovery decision-making. If the flywheel operates in the normal SOC interval (0.25–0.85) but is predicted to drop to the charging recovery zone (0.20–0.25) within the prediction horizon, early low-power charging is performed following Equation (27). If it is predicted to reach the discharge recovery range beforehand, advanced low-power discharging is executed according to Equation (28).

A prediction-based correction item is superimposed on the SOC feedback control loop to further limit the charging and discharging coefficients.

$$\begin{cases} \mathrm{k}'_{\mathrm{d}} = \mathrm{k}_{\mathrm{d}} \left(\phi \cdot \frac{\min\left(\mathrm{SOC}_{\mathrm{temp}}(\mathrm{i})\right) - \mathrm{SOC}_{\mathrm{min}}}{\delta_{\mathrm{th}}} \right) & ,\psi_L = 1 \\ \mathrm{k}'_{\mathrm{c}} = \mathrm{k}_{\mathrm{c}} \left(\phi \cdot \frac{\mathrm{SOC}_{\mathrm{max}} - \max\left(\mathrm{SOC}_{\mathrm{temp}}(\mathrm{i})\right)}{\delta_{\mathrm{th}}} \right) & ,\psi_H = 1 \end{cases} \tag{28}$$

where k'_{c} and k'_{d} are the charge–discharge coefficients under the battery energy storage prediction constraints; ϕ is the confidence level of the prediction model's output, set to 0.8.

After updating the charge and discharge coefficients, the SOC is dynamically adjusted according to Equations (22) and (23).

2.4. Model Evaluation Methods

2.4.1. Power Prediction Evaluation Metrics

To comprehensively and objectively quantify the prediction performance of the proposed model, two quantitative evaluation systems are adopted: prediction accuracy indicators and tracking accuracy indicators. Furthermore, the practical engineering applicability of the model is verified by incorporating the SOC constraint of the energy storage system. The computational formula and physical interpretation of each evaluation index are given as follows [16]:

1. Root Mean Square Error (RMSE);

Measures the overall deviation between predicted and actual values, reflecting the model's overall prediction accuracy:

$$RMSE = \sqrt{\frac{1}{n}\sum_{k=1}^{n}\left(P_{d_fore}(k) - P_d(k)\right)^2} \tag{29}$$

where n is the data length; $P_{d_fore}(k)$ is the predicted value at time k; $P_d(k)$ is the actual value at time k.

2. Mean Absolute Error (MAE);

Reflects the average level of prediction error and avoids the issue of positive and negative errors canceling each other out:

$$MAE = \frac{1}{n}\sum_{k=1}^{n}\left|P_{d_fore}(k) - P_d(k)\right| \tag{30}$$

3. Tracking Error (TE).

Evaluates the model's ability to track power trend changes, reflecting dynamic adaptability:

$$TE = \frac{1}{n-1}\sum_{k=2}^{n}\left|\left(P_{d_fore}(k) - P_{d_fore}(k-1)\right) - \left(P_d(k) - P_d(k-1)\right)\right| \tag{31}$$

2.4.2. Frequency Regulation Performance Metrics

A typical procedure of a TPU responding to AGC commands can be illustrated with Figure 6.

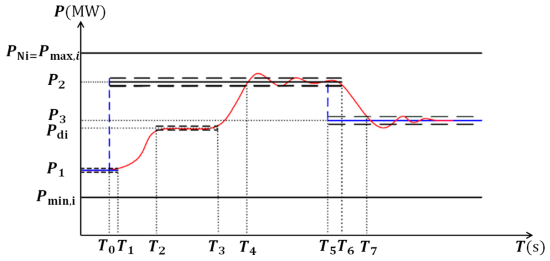

Figure 6. Typical AGC dynamic response process of the TPU.

As shown in Figure 6, the unit operates steadily at P_1 before T_0, follows the P_2 upward AGC command issued at T_0, crosses the deadband at T_1, completes coal mill startup P_{di} at T_3, and settles within the P_2 deadband after slight power fluctuations. After the command switches to P_3 at T_5, the unit passes the deadband at T_6 and stabilizes near P_3. P_{max} and P_{min} represent the maximum and minimum adjustable power limits.

The metrics used to evaluate the unit's AGC performance are defined as follows: according to the Shandong Power Grid's calculation method for the single frequency regulation performance indicator in the frequency regulation auxiliary market, the unit's participation in the AGC frequency regulation ramp-up performance assessment involves the following metrics, which calculate the unit's comprehensive frequency regulation performance based on three performance factors: rate, time, and accuracy [9].

1. Regulation rate K_1.

This represents the rate at which the unit increases output toward the AGC command, gradually transitioning from the point where the unit crosses the coal-grinding point, through the 1% Pe MW response deadband, to the 1% Pe MW point beyond the regulation deadband. It is defined as the absolute value of the slope of the connecting line. The actual rate is calculated using Equation (32), K_1, with a maximum value of 2, as shown in Equation (33):

$$\nu = \left|\frac{P_{id} - P_{ed}}{T_{id} - T_{ed}}\right| \times 100\% \tag{32}$$

$$K_1 = 2 - \frac{\nu}{\nu_N} \tag{33}$$

where ν represents the regulation rate achieved by the unit during the regulation process; furthermore, ν_N represents the unit's standard regulation rate (MW/min), which is 1.5% of the rated active power for pulverized coal-fired units and 1% of the rated active power for circulating fluidized bed units.

2. Regulation accuracy K_2.

This refers to the difference between the actual output power and the setpoint power fluctuating within the deadband after the unit's response has stabilized. The absolute value of this difference is integrated and divided by the integration time to obtain the regulation deviation for that time period, as shown in Equation (34):

$$\Delta P = \frac{\int_{T_s}^{T_e} |P(t) - P_S| \times dt}{T_e - T_s} \tag{34}$$

where ΔP is the unit power deviation; $P(t)$ is the actual output power during that time period; P_S is the setpoint power value; T_s is the end time of the command; and T_e is the start time of the control deadband. The regulation accuracy k_2 calculation formula is as follows (20):

$$K_2 = 2 - \frac{\Delta P}{\Delta P_N} \tag{35}$$

where the permitted control deviation ΔP_N is 1% of the unit's rated active power.

3. Response rate K_3.

This refers to the time it takes for the unit, after receiving an AGC command, to begin output and move in the same direction as the TPU's output.

$$K_3 = 2 - \frac{T_f - T_i}{T_N} \tag{36}$$

where T_f is the dead-time for the overshoot response; T_i is the time to reach the response, and T_N is the standard response time; the standard response time for a TPU is less than 1 min.

4. Comprehensive frequency regulation performance index K_p.

This is the product of individual performance indices, representing the balanced proportion of the three indices, and measures the quality of the frequency regulation resource's regulation performance.

$$K_p = K_1 * K_2 * K_3 \tag{37}$$

3. Results and Analysis

To verify the accuracy of the proposed prediction model, real operational data of a TPU for frequency regulation located in Shandong, China, are used for validation. The unit possesses an installed capacity of 330 MW. Its power data sampling interval and control cycle are both 1 s, and it takes part in AGC frequency regulation all day long. Table 1 shows which physical signals were collected in Section 4. All simulations and data analyses were implemented in MATLAB.

First, statistical analysis is conducted on raw power data. Figure 7 presents the distribution of energy storage demand power for AGC frequency regulation. The power fluctuation range is -20 MW to 20 MW, where 98.9% of sampling points fall within the ± 15 MW band. Therefore, the demanded power is discretized at intervals of 1/3 MW to establish a Markov probability transition matrix.

Simulation parameters are presented in Table 2. The capacity configurations of the flywheel and lithium battery listed in the table are determined according to the actual

frequency modulation requirements of the system. The number of discrete states s is obtained based on a fixed parameter resolution. Both the adaptive learning parameters λ and maximum nodes π_{max} are set as fixed values in this study, which can be further optimized and adjusted in subsequent research. In addition, the dynamic self-recovery coefficient m, flywheel self-recovery coefficient k_f, and battery self-recovery coefficient k_b are configured on the basis of comprehensive sensitivity analysis.

Table 1. Types of physical signals collected in Section 4.

Signal	Symbol	Type	Role
AGC command	P_{AGC}	Measured	Dispatch reference
Thermal-unit active power	P_{TPU}	Measured	Actual unit response
HESS demand power	P_c	Derived	$P_{AGC} - P_{TPU}$
Discrete HESS demand states	P_d	Derived	Model input
FESS/BESS power	P_f, P_b	Simulated	Control outputs
FESS/BESS SOC	S_f, S_b	Simulated state	Constraint and life assessment
AGC command	P_{AGC}	Measured	Dispatch reference
Thermal-unit active power	P_{TPU}	Measured	Actual unit response

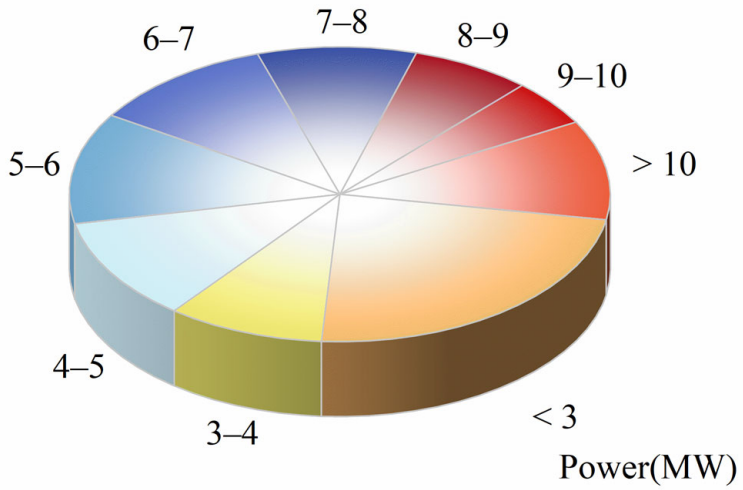

Figure 7. Distribution of HESS required regulation power.

Table 2. Simulation parameter settings.

Parameter	Value
Adaptive learning parameters λ	1.2
Number of discrete states s	120
maximum nodes π_{max}	40
FESS capacity	5 MW/2 MWh
BESS capacity	10 MW/10 MWh
Dynamic self-recovery coefficient m	2
Flywheel self-recovery coefficient k_f	0.8
Battery self-recovery coefficient k_b	0.8

3.1. Effectiveness of the Three-Matrix Model

The Markov transition matrix of the HESS demand power is shown in Figure 8.

As shown in Figure 8a–d, most state transition probabilities are concentrated on the diagonal elements of the heatmaps. For the rising-state matrix, relatively high probabilities appear on the right side of the main diagonal, whereas the falling-state matrix presents elevated values on the left diagonal region.

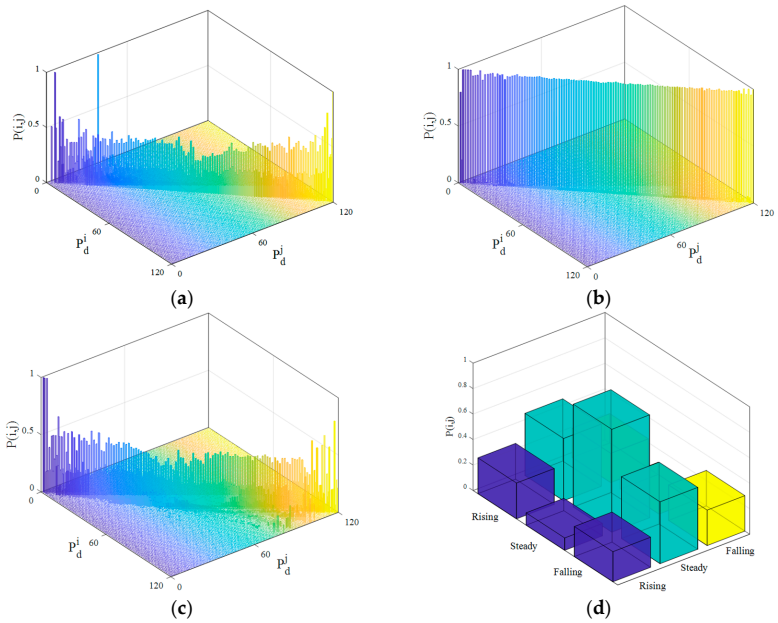

Figure 8. Markov transition probability matrices and trend transition characteristics: (**a**) increasing demand power; (**b**) stable demand power; (**c**) decreasing demand power; and (**d**) trend in demand power.

Five-step power prediction is implemented following the adaptive strategy proposed in Section 2. Partial comparisons between the five-step predicted demand power and actual power are illustrated in Figure 9. Owing to the stochasticity and memoryless property of Markov chains, multi-step predicted values can be derived via matrix multiplication. As derived from Equation (2), multi-step prediction probabilities gradually disperse with the extension of prediction horizons, and the probability discrepancy among various scenarios diminishes. Simply adopting the maximum-probability scenario will enlarge prediction errors. Therefore, this work combines adaptive updating of Markov matrices and weighted random sampling to construct a scenario tree for prediction accuracy improvement. Table 3 summarizes the prediction accuracy under different adaptive time spans D_T, and Table 3 presents accuracy comparisons among different scenario selection methods.

Table 3. Impact of different adaptive times on prediction accuracy.

Adaptation Time (h)	RMSE (MW)	Accuracy Improvement (%)
0	0.7981	—
1	0.7818	2.04
2	0.7785	2.46
3	0.7802	2.24
4	0.7804	2.22
5	0.7804	2.22
6	0.7802	2.24

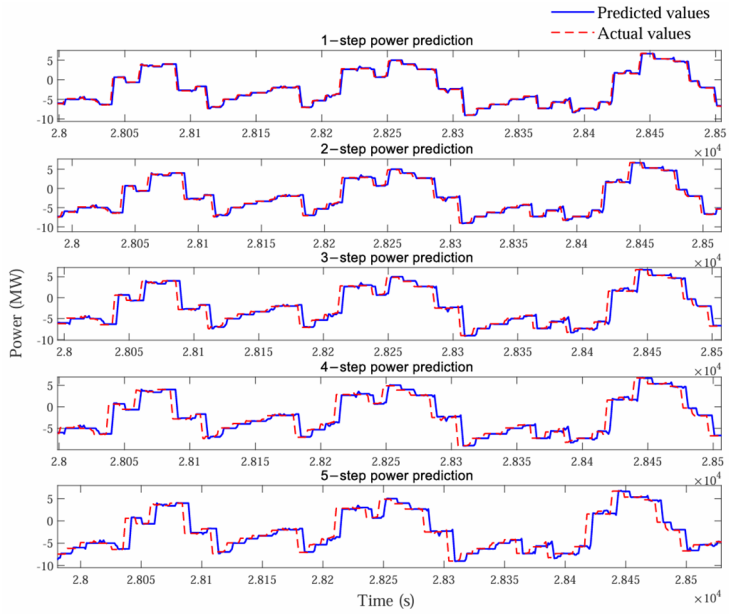

Figure 9. Five-step prediction t tracking results (partial).

It can be seen from Figure 9 that prediction accuracy deteriorates gradually with the increase in prediction steps. Nevertheless, the predicted series can generally track the actual power demand of the HESS, which validates that the trend-driven triple-matrix Markov chain model achieves reliable prediction accuracy for HESS load time series.

Comparative results in Table 3 reveal that the optimal adaptive update interval is determined as 2 h, which achieves the maximum accuracy improvement of 2.46% compared with the Markov model without online adaptive updating. In practical power grid dispatch, AGC frequency regulation instructions fluctuate periodically, driven by hourly grid load variations, which well matches the optimized 2 h update window in this work. Consequently, the 2 h adaptive window can effectively capture the periodic fluctuation characteristics of AGC regulation commands. Candidate update intervals of 0–6 h with a 1 h increment were evaluated on the validation subset. The interval yielding the lowest validation RMSE, namely, 2 h, was selected and then fixed during testing.

Given the obvious performance gaps among various scenario tree generation algorithms, controlled variable comparative experiments are carried out, and quantitative results are summarized in Table 4. Different from the conventional MLE-based scenario tree method, the proposed variable time-domain weighted random sampling uniformly selects candidate nodes over the complete probability density function. This mechanism ensures that sampled scenarios maintain high occurrence probabilities across diverse prediction horizons. In addition, the probability gaps among alternative scenarios narrow with the extension of prediction steps (e.g., the fifth-step prediction), allowing the algorithm to reserve more representative low-probability operation scenarios. Statistical results demonstrate that the proposed method reduces RMSE by 4.45% compared with fixed-topology scenario trees and by 3.87% compared with the MLE method. Such improvements overcome two inherent drawbacks of benchmark models: the excessive computational cost of fixed-structure scenario trees and the single-path selection limitation of MLE, thereby lifting the overall prediction accuracy of HESS power demand.

Table 4. Impact of different scenario tree generation methods on prediction accuracy.

Method	RMSE (MW)	Accuracy Improvement (%)
Fixed scenario tree	0.8159	----
Proposed weighted random sampling method	0.7793	4.45
Maximum likelihood estimation (MLE)	0.8107	0.64

Performance Validation of K-means Time-Series Morphology Clustering Correction Strategy.

Silhouette coefficients under different cluster numbers K are computed as follows:

As shown in Table 5, K = 2 is the one with the largest coefficient. The outputs from the Markov chain module are further corrected via a historical-data revision strategy based on K-means clustering, and its quantitative enhancement is listed in Table 6.

Table 5. Silhouette coefficient for different numbers of clusters.

K Value	2	3	4	5	6
Silhouette coefficient	0.3997	0.3267	0.2894	0.2337	0.2171

Table 6. Impact of clustering correction on prediction accuracy.

Method	RMSE (MW)	Accuracy Improvement (%)
Without clustering correction	0.7793	—
Correction of cluster number 2	0.6418	17.64
Correction of cluster number 3	0.6105	21.66
Correction of cluster number 4	0.6059	22.25
Correction of cluster number 5	0.6647	14.71
Correction of cluster number 6	0.6256	20.44

A real-time waveform matching framework embedded with an adaptive updating mechanism is designed in this study. During rolling prediction, fixed-length sliding windows are utilized to extract segmented features from time-series samples at each sampling instant. A three-segment (front–middle–rear) average deviation discrimination rule is adopted to identify curve morphological patterns, which fully excavates global window features and suppresses the interference of isolated outliers. After measuring the similarity between the real-time waveform and four typical power profile clusters W_k, the cluster with the highest conditional similarity is screened out. Historical samples featuring similar power operating levels within the matched cluster are retrieved, and their average value is taken as the real-time correction term for predicted power [23]. As indicated in Table 6, the correction of cluster number 4 achieves a 22.25% reduction in RMSE. This post-processing strategy compensates for the intrinsic limitation originating from the memoryless property of pure Markov chains and significantly strengthens overall prediction reliability [24].

Considering the characteristics of power demand data for HESS, classification using K = 2 only roughly divides the data into rising and falling power demand categories, ignoring

the characteristic pattern of a steady phase followed by a sudden change; failing to fully utilize the data hinders subsequent refinement. However, K = 4, though with a slightly lower coefficient, can significantly distinguish four typical operating conditions, and subsequent curve screening can compensate for the noise introduced by shape segmentation, thereby demonstrating the overall optimality of K = 4 for engineering applications. Ultimately, a K = 4 classification strategy was adopted, balancing the silhouette coefficient with sample patterns, and categorizing the power demand data into rising, falling, peak-type (rising first, then steady, and finally falling), and valley-type (falling first, then steady, and finally rising). The plots for these four data categories are shown in Figure 10.

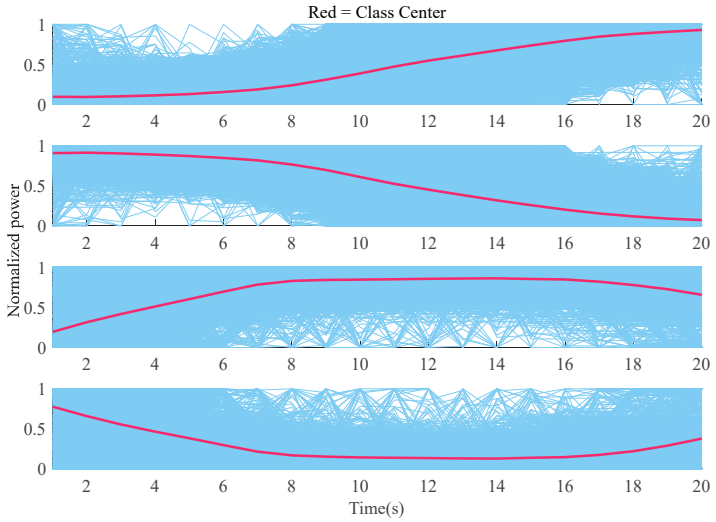

Figure 10. Clustering by different patterns.

3.2. Validation of Dynamic-Interval SOC Control Strategy

Relying on multi-step-ahead predicted power sequences, an SOC-friendly dynamic-interval feedforward-feedback coordinated control strategy is proposed. This method pre-calculates SOC evolution trends within the prediction horizon and implements proactive regulation in advance. Such a feedforward closed-loop control architecture effectively prevents lithium-ion batteries from suffering rapid deep SOC depletion.

Figure 11 compares SOC trajectories between the traditional hard-limiting clamping control and the proposed control framework. The conventional strategy only maintains battery SOC within the optimal operation range for 43.97% of the whole operation period, whereas the dynamic-interval feedforward strategy increases this ratio to 59.03%, corresponding to a relative improvement of 34.25%. The clamping control suffers from evident response delay during SOC decline processes, forcing batteries to operate at low SOC levels under peak power demand and weakening their AGC frequency regulation tracking capability. In contrast, the proposed method executes pre-regulation before SOC drops via power prediction, combined with dynamic SOC interval management for battery packs, which remarkably prolongs the duration that SOC stays within the safe optimal window.

As shown in Table 7, the rainflow counting algorithm is adopted to quantify the daily equivalent cycle numbers of lithium-ion batteries participating in full-day AGC. For a standalone battery energy storage system with the same rated parameters (15 MW/12 MWh) as the HESS, the daily equivalent cycle count reaches 7.0128. Under conventional control, this value decreases to 4.6374 cycles, and the proposed strategy further reduces it to 3.7190 cycles, achieving a 19.80% extension of battery cycle life.

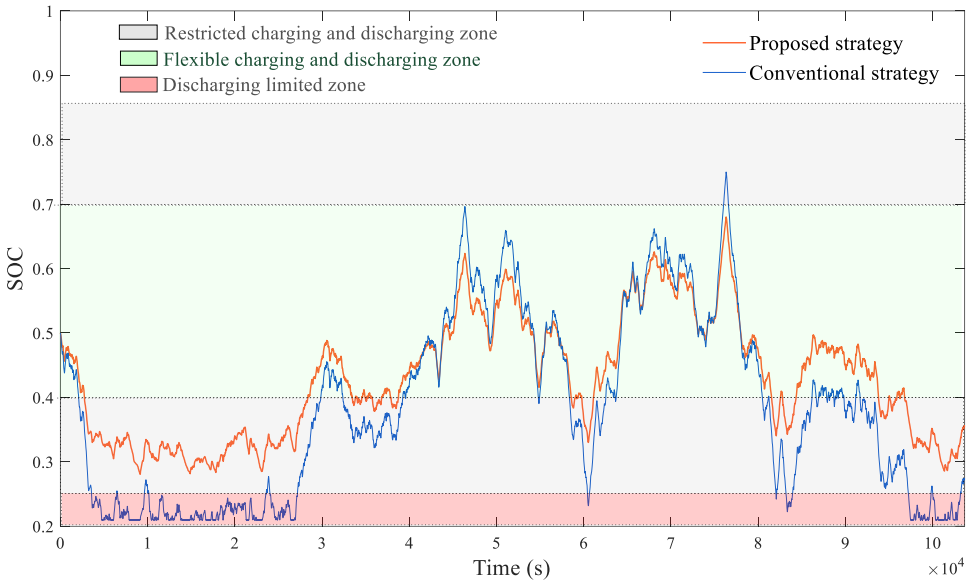

Figure 11. SOC evolution curves under different control strategies.

Table 7. Statistical daily equivalent cycle counts of lithium-ion batteries.

Item	Equivalent Cycle Count (Cycles)	Lifespan Extension (%)
Single battery energy storage	7.0128	—
Conventional control strategy	4.6374	33.87
Proposed control strategy	3.7190	46.97

3.3. Comprehensive AGC Frequency Regulation Performance Validation of TPU

Figures 12 and 13 present the AGC command tracking curves of both the conventional strategy and the proposed strategy under step commands of the same magnitude. In Figure 12, consecutive step-up AGC commands are issued. The proposed strategy achieves a rapid response to the AGC command and delivers higher tracking accuracy. In contrast, the output power of the conventional strategy drops significantly as the energy storage SOC enters the limit interval, resulting in a large tracking deviation. In Figure 13, step-down AGC commands are applied. The proposed strategy outperforms the conventional strategy in both response time and tracking error.

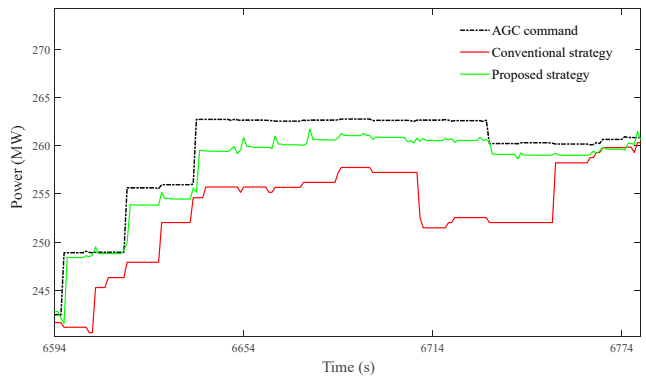

Figure 12. AGC step-up command tracking performance under two control strategies.

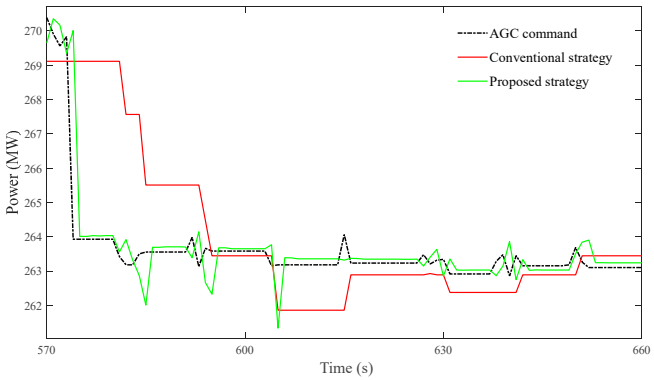

Figure 13. AGC step-down command tracking performance under two control strategies.

The results verify that the proposed dynamic SOC interval management strategy can maintain BESS capacity within the safe operating range, providing reliable support for secondary frequency regulation tasks. Meanwhile, the strategy of prioritizing FESS to undertake small-amplitude high-frequency power commands helps reduce the system response time to AGC commands. Detailed comparisons of frequency regulation performance metrics are provided in Figure 14.

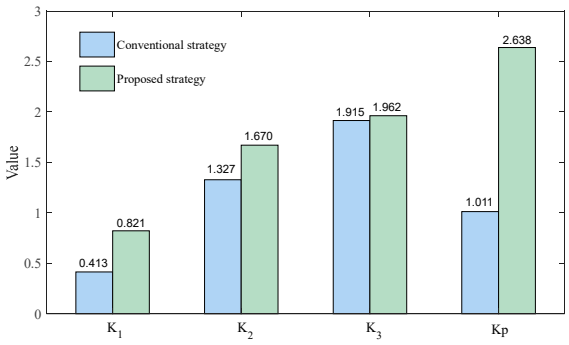

Figure 14. Comparison of average frequency regulation performance.

Figure 14 shows a comparison of frequency regulation performance metrics under different strategies. The strategy proposed in this paper achieves improvements of 98.64%, 25.80%, and 2.43% in K_1 (regulation rate), K_2 (regulation accuracy), and K_3 (response time), respectively. Ultimately, it achieves a 160.93% improvement in K_P, indicating that the strategy proposed in this paper is more effective at tracking AGC commands and completing frequency regulation tasks.

Figure 15 presents a comparative analysis of the unit's continuous AGC command tracking performance. The test adopts an on-site AGC dispatch sequence covering typical composite operating conditions, including ramp-up, ramp-down, load turnaround, and high-frequency small-amplitude fluctuations, to comprehensively evaluate the dynamic performance of the control strategies under continuous frequency regulation scenarios. As can be seen, the conventional strategy tends to trigger hard limiting due to SOC limit violations during rapid load turnaround and sustained ramp stages, leading to notable tracking lag, enlarged deviation, and even reverse power regulation, which undermines the overall frequency regulation quality. By contrast, the proposed strategy, enabled by multi-step prediction feedforward and dynamic SOC interval management, maintains BESS SOC within the safe operating range throughout the test with no hard cutoff occurrence. With FESS preferentially undertaking high-frequency power components, the strategy achieves faster dynamic response at command inflection points and smaller steady-state tracking

deviation during ramp processes, realizing accurate and smooth tracking of continuous AGC commands.

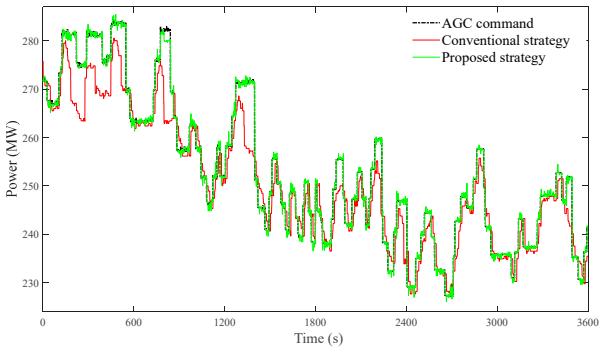

Figure 15. Continuous AGC command tracking curves in partial operation periods.

3.4. Performance Verification and Sensitivity Analysis

This section further validates the proposed method from three perspectives: comparison of power prediction models, comparison of control strategies, and parameter sensitivity analysis.

3.4.1. Comparison of Power Prediction Models

To benchmark the prediction accuracy of the proposed three-matrix adaptive Markov model, it is compared with LSTM, GRU, a randomized model predictive control (RandomMPC) approach, and ARIMA on the same HESS demand dataset using RMSE, MAE, and TE as evaluation metrics [25,26]. The results are listed in Table 8.

Table 8. Comparison of prediction accuracy among prediction models.

Model	RMSE (MW)	MAE (MW)	TE (MW)
LSTM	0.70813	0.36547	0.47377
GRU	0.69721	0.34230	0.51340
RandomMPC	0.71373	0.39835	0.63291
ARIMA	0.77673	0.28149	0.33808
Proposed Markov model	0.60590	0.25170	0.35000

As shown in Table 8, the proposed model achieves the lowest RMSE (0.6059) and MAE (0.2517), which are approximately 13.1% and 10.6% lower than the best-performing baseline on each metric, respectively. Although ARIMA attains a slightly lower TE (0.3381) than the proposed model (0.3500), it suffers from markedly larger RMSE and MAE, indicating that its apparent advantage in tracking trend reversals is offset by large steady-state deviations. The data-driven LSTM and GRU models and the RandomMPC approach yield uniformly higher errors across all three metrics. Overall, the proposed Markov-based predictor provides the most accurate and reliable short-term HESS demand forecast under the non-stationary AGC regulation pattern.

3.4.2. Comparison of Control Strategies

To further verify the proposed HESS coordinated control strategy, it is compared with four representative strategies under the same AGC command sequence: a rule-based strategy (RULE), a linear model predictive controller (MPC), a conventional hard-limiting SOC clamping strategy, and a single battery energy storage scheme. The five regulation metrics

introduced in Section 2.4 and the daily equivalent battery cycle count are summarized in Table 9.

It can be observed from Table 9 that the proposed strategy attains the highest comprehensive performance index K_p of 2.638, which is 160.9%, 84.5%, and 17.6% higher than the conventional, MPC, and RULE strategies, respectively, and 242.6% higher than the single-battery scheme. Meanwhile, the daily equivalent cycle count is reduced to 3.7190, which is 19.8%, 23.2%, and 35.2% lower than the conventional, MPC, and RULE strategies, and 47.0% lower than the standalone battery system. The improvement is most pronounced in K_1 (regulation rate), where the proposed strategy reaches 0.821—roughly twice that of the conventional strategy—because the flywheel-assisted fast power response compensates for the large dead-time imposed by coal mill and boiler inertia. These results confirm that the prediction-driven dynamic SOC interval control simultaneously enhances AGC regulation quality and extends battery service life.

Table 9. AGC performance and battery life comparison across control strategies.

Strategy	K_1	K_2	K_3	K_p	Equivalent Cycle Count (Cycles)
Proposed Markov model	0.821	1.670	1.962	2.638	3.7190
RULE	0.712	1.630	1.933	2.243	5.7394
MPC	0.581	1.254	1.932	1.430	4.8450
Conventional control strategy	0.413	1.327	1.915	1.011	4.6374
Single battery energy storage	0.378	1.120	1.833	0.770	7.0128

3.4.3. Parameter Sensitivity Analysis

The proposed strategy involves five tunable hyperparameters: the BESS self-recovery exponent m, the flywheel self-recovery coefficient K_f, the battery self-recovery coefficient K_b, the prediction confidence level ϕ, and the SOC warning threshold δ_{th}. A one-factor-at-a-time (OFAT) analysis is conducted to examine whether the above conclusions hold when these parameters deviate from their nominal values. Each parameter is perturbed to three representative levels while the others are fixed; the resulting K_p, optimal SOC percentage, and corrected equivalent cycle count are listed in Figure 16.

Figure 15 shows the comprehensive AGC performance index, optimal SOC percentage, and corrected equivalent cycle count under the investigated parameter settings. As shown in Figure 16, the optimal SOC percentage remains between 56.16% and 61.25%, and the equivalent cycle count stays between 3.67 and 3.78 cycles across all cases, indicating that the strategy is inherently robust. Parameter K_f exerts negligible performance impact. Since it only adjusts flywheel standby power for fast small-amplitude compensation, perturbing K_f from 0.6 to 1.0 barely changes SOC, cycle count, or K_p (variation < 1%). Parameters K_b and m also produce mild responses: K_p deviates by no more than 6%, with SOC and cycling metrics staying close to nominal results. By contrast, δ_{th} and ϕ are the most sensitive hyperparameters. Increasing δ_{th} to 0.07 widens the SOC early-warning band, postponing pre-recovery triggers and letting battery SOC approach hard limits, which reduces K_p to 2.413. Reducing ϕ to 0.6 yields conservative feedforward correction and slightly degrades K_p to 2.491; increasing ϕ to 1.0 elevates K_p to 2.681 yet raises battery cycling intensity to 3.6744, as aggressive prediction-driven correction compresses the available operating range for batteries. Hence, nominal settings $\phi = 0.8$ and $\delta_{th} = 0.05$ achieve a good trade-off between AGC regulation capability and battery service-life performance.

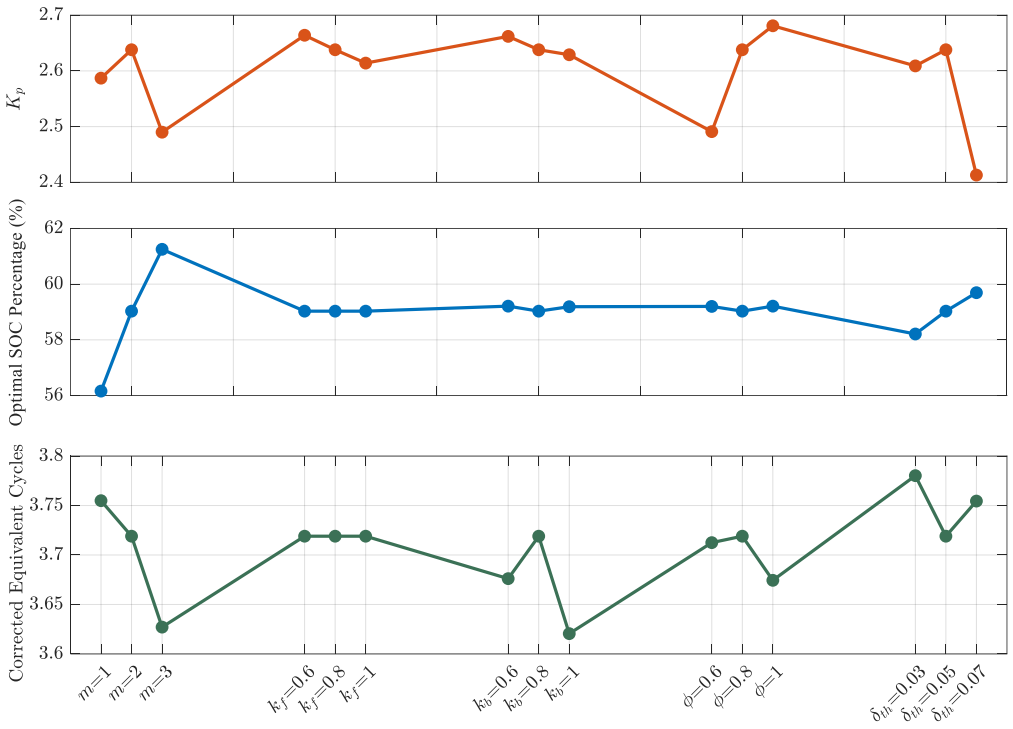

Figure 16. Sensitivity analysis of key control hyperparameters.

4. Conclusions

The adaptive Markov model serves as the core prediction engine of the proposed framework, providing the probabilistic multi-step HESS demand-power information required by the subsequent optimization and control modules. The core innovations and experimental findings of this study are condensed into five conclusive points:

1. An adaptive online updated triple-matrix Markov chain prediction framework corrected by K-means clustering is constructed, together with a HESS coordinated AGC control strategy. The high-precision power prediction module provides reliable input sequences for the closed-loop optimal control system.
2. Taking RMSE as the quantitative evaluation standard, the proposed three-matrix Markov chain model improves prediction accuracy by 4.56% compared with the traditional dual-matrix model and by 10.35% compared with the single-matrix model. The optimal adaptive update interval is determined to be 2 h for the studied case. The online adaptive updating mechanism brings a 2.36% accuracy increment against fixed-parameter Markov models and adapts well to periodic fluctuations of AGC regulation instructions.
3. The weighted random sampling scenario tree generation method outperforms the MLE algorithm by 3.87% and fixed-topology scenario trees by 4.45% in prediction accuracy, while effectively reducing computational complexity.
4. A historical similar waveform matching correction method is proposed. Typical power profile clusters W_k and a historical correction database are established via the K-means clustering algorithm. Real-time morphological similarity matching is adopted to adaptively revise predicted values, further reducing RMSE by 22.25%.
5. Supported by the foregoing prediction module, proactive pre-regulation is realized for the HESS. The dynamic-interval SOC feedforward-feedback control increases the proportion of battery SOC operating within the optimal range by 34.25%, extends the cycle life of lithium-ion batteries by 19.80%, and raises the comprehensive frequency regulation performance index k_p by 160.93%.

This study is limited by the use of data from one thermal power plant and by simulation-based validation of the HESS internal states. The fixed hyperparameters and the post-event degradation assessment do not represent a fully adaptive life-aware optimization framework. Future work will validate the method using multi-plant and multi-season AGC datasets, incorporate online uncertainty quantification and degradation-cost estimation, and establish formal closed-loop stability guarantees for the prediction-assisted controller.

Author Contributions: Writing—original draft, conceptualization, and project administration: J.T. and M.W.; writing—original draft, software, and investigation: Z.Y.; writing—review and editing and supervision: F.H.; writing—review and editing and investigation: J.F., Q.J., D.P., and Y.S. All authors have read and agreed to the published version of the manuscript.

Funding: This work was supported by the Science and Technology Program of State Grid Corporation of China (SGCC) under Grant 522201250016-250-YYGG.

Data Availability Statement: The original contributions presented in this study are included in the article; further inquiries can be directed to the corresponding author.

Conflicts of Interest: Authors J.T. and M.W. were employed by the State Grid Liaoning Electric Power Co., Ltd. Authors Z.Y., Q.J., D.P., and Y.S. were employed by the State Grid Liaoning Electric Power Research Institute. The authors declare that this study received funding from the Science and Technology Program of State Grid Corporation of China (SGCC). The funder was not involved in the study design, collection, analysis, interpretation of data, the writing of this article, or the decision to submit it for publication. The remaining authors declare that the research was conducted in the absence of any commercial or financial relationships that could be construed as a potential conflict of interest.

Abbreviations

The following abbreviations are used in this manuscript:

SOC	State of Charge
HESS	Hybrid Energy Storage System
BESS	Battery Energy Storage System
FESS	Flywheel Energy Storage System
TPU	Thermal Power Units

References

1. National Energy Administration of China. 2025 Annual Report on China's Electricity Market Development. Available online: https://www.nea.gov.cn/20260609/2d1bf220b5a642e2b1199a015bd6cf13/c.html (accessed on 15 August 2026).
2. Zhuo, Z.Y.; Zhang, N.; Xie, X.R.; Li, H.Z.; Kang, C.Q. Key Technologies and Development Challenges for Power Systems with a High Proportion of Renewable Energy. *Autom. Electr. Power Syst.* **2021**, *45*, 171–191.
3. Zheng, L.F.; Miao, Y.C.; Teng, X.B.; Mi, H.N.; Xu, C.K.; Yan, Z.; Li, C.B.; Chen, S.J. Model and Method for Flexibility Retrofit of Thermal Power Units Considering Energy Storage Allocation. *Proc. CSEE* **2025**, *45*, 1501–1513. [CrossRef]
4. Dongxu, H.; Xingjian, D.; Wen, L.; Yangli, Z.; Xuehui, Z.; Haisheng, C.; Zhilai, Z. A Review of Flywheel Energy Storage Rotor Materials and Structures. *J. Energy Storage* **2023**, *74*, 109076. [CrossRef]
5. Hong, F.; Jia, X.Y.; Liang, L.; Hao, J.H.; Fang, F.; Liu, J.Z. Hierarchical Capacity Optimization of Hybrid Energy Storage for Frequency Support in Wind Farms. *Proc. CSEE* **2024**, *44*, 5596–5607. [CrossRef]
6. Latif, A.; Hussain, S.M.S.; Das, D.C.; Ustun, T.S. State-of-the-Art of Controllers and Soft Computing Techniques for Regulated Load Frequency Management of Single/Multi-Area Traditional and Renewable Energy Based Power Systems. *Appl. Energy* **2020**, *266*, 114858. [CrossRef]
7. Sun, B.Y.; Liu, Z.Q.; Yang, S.L.; Wang, R.; Li, T.T. Joint AGC Strategy of Energy Storage and Thermal Power with Real-Time Optimization of Compensation Degree. *Power Syst. Technol.* **2018**, *42*, 426–436. [CrossRef]
8. Hong, F.; Du, H.; Liang, L.; Zhang, Y.; Fang, F.; Liu, J.Z. Control Strategy and Application of Flywheel/Lithium Battery Hybrid Energy Storage Assisted Thermal Power AGC Based on Modal Matching. *Proc. CSEE* **2026**, *46*, 2229–2240. [CrossRef]

9. Xie, X.; Guo, Y.; Wang, B.; Dong, Y.; Mou, L.; Xue, F. Improving AGC Performance of Coal-Fueled Thermal Generators Using Multi-MW Scale BESS: A Practical Application. *IEEE Trans. Smart Grid* **2018**, *9*, 1769–1777. [CrossRef]
10. Yuan, M.; Tian, L.; Jiang, T.; Hu, R.; Cui, X. Research on the Capacity Configuration of the "Flywheel + Lithium Battery" Hybrid Energy Storage System That Assists the Wind Farm to Perform a Frequency Modulation. *J. Phys. Conf. Ser.* **2022**, *2260*, 012026. [CrossRef]
11. Sun, B.; Zhao, H.; Xie, M.; Li, B. Design of Energy Management for Composite Energy Storage System Consisting of Lithium Battery and Flywheel Based on Adaptive Wavelet–Fuzzy Control Strategy. *J. Braz. Soc. Mech. Sci. Eng.* **2024**, *46*, 434. [CrossRef]
12. Wang, T.Y.; Zhang, J.F.; Yin, H.R.; Zhang, X.J.; Zhao, H.Y.; Wang, Q.; Li, Q. Stochastic Model Predictive Control for Hybrid Energy Storage Assisted Thermal Power Unit AGC Based on Adaptive Markov Power Prediction. *Therm. Power Gener.* **2026**, *55*, 147–157. [CrossRef]
13. He, J.Q.; Shi, C.L.; Wei, T.Z. Adaptive Energy Storage Demand Power Prediction Model Based on Markov Chain. *Trans. China Electrotech. Soc.* **2021**, *36*, 563–571. [CrossRef]
14. Ma, Z.H.; Li, X.R.; Tan, Z.X.; Huang, J.Y.; He, K. Primary Frequency Regulation Control Method Considering Dead Band of Energy Storage Frequency Regulation. *Trans. China Electrotech. Soc.* **2019**, *34*, 2102–2115. [CrossRef]
15. Shen, J.Y.; Zhang, F.F. Power Demand Prediction Based on Adaptive Online Learning of Markov Model. *Microcomput. Appl.* **2026**, *42*, 64–67.
16. Li, Y.; Yang, M.; Su, X. Short-Term Photovoltaic Power Prediction Based on Ensemble Clustering and Improved Markov Chain Model. *South. Power Syst. Technol.* **2023**, *17*, 113–122. [CrossRef]
17. Dong, L.; Liu, M.X.; Chen, N.S.; Fan, S.X.; Pu, T.J. Coordinated Optimization Control of Distributed Energy Resources Based on Stochastic Model Predictive Control. *Power Syst. Technol.* **2018**, *42*, 3219–3227. [CrossRef]
18. Liu, J.; Lin, S.J.; Liang, W.K.; Wang, Q.; Liu, M.B. Short-Term Probabilistic Prediction of Photovoltaic Output Based on High-Order Markov Chain and Gaussian Mixture Model. *Power Syst. Technol.* **2023**, *47*, 266–275. [CrossRef]
19. Zhu, C.X.; Zhang, Y.; Yan, Z.; Zhu, J.Z.; Zhao, T. Wind Power Time Series Modeling Using Improved Markov Chain Monte Carlo Method. *Trans. China Electrotech. Soc.* **2020**, *35*, 577–589. [CrossRef]
20. Tang, J.; Li, X.R.; Huang, J.Y.; Xu, P.; He, C. Capacity Configuration Method of Energy Storage Batteries Participating in Secondary Frequency Regulation with the Objective of Maximizing Net Benefit. *Trans. China Electrotech. Soc.* **2019**, *34*, 963–972. [CrossRef]
21. Xie, Z.J.; Li, D.X.; Wang, J.R.; Meng, T. Research on Application Scenarios and Control Methods of Energy Storage Systems for Power System Frequency Regulation. *Therm. Power Gener.* **2020**, *49*, 117–125. [CrossRef]
22. Shi, Y.; Xu, B.; Tan, Y.; Zhang, B. A Convex Cycle-Based Degradation Model for Battery Energy Storage Planning and Operation. In Proceedings of the 2018 American Control Conference, Milwaukee, WI, USA, 27–29 June 2018. [CrossRef]
23. Zhang, S.; Yang, J.X.; Liu, J.C.; Liu, J.Y.; Lin, H.Z. Power Load Data Reconstruction Based on Multiscale Time-Series Modeling and Estimation. *Trans. China Electrotech. Soc.* **2020**, *35*, 2736–2746. [CrossRef]
24. Guan, L.; Zhao, Q.; Zhou, B.R.; Lü, Y.T.; Zhao, W.M.; Yao, W.F. Modeling and Forecasting of Photovoltaic Power Characteristics Based on Multiscale Cluster Analysis. *Autom. Electr. Power Syst.* **2018**, *42*, 24–30.
25. Liu, X.; Lin, Z.; Feng, Z. Short-Term Offshore Wind Speed Forecast by Seasonal ARIMA—A Comparison Against GRU and LSTM. *Energy* **2021**, *227*, 120492. [CrossRef]
26. Amalou, I.; Mouhni, N.; Abdali, A. Multivariate Time Series Prediction by RNN Architectures for Energy Consumption Forecasting. *Energy Rep.* **2022**, *8*, 1084–1091. [CrossRef]

Disclaimer/Publisher's Note: The statements, opinions and data contained in all publications are solely those of the individual author(s) and contributor(s) and not of MDPI and/or the editor(s). MDPI and/or the editor(s) disclaim responsibility for any injury to people or property resulting from any ideas, methods, instructions or products referred to in the content.